Non-invasive imaging platform reveals a potential tumourigenicity hazard of systemically administered cells

Authors: Lauren Scarfe[1, 2, §], Arthur Taylor[1, 2, §], Jack Sharkey[1, 2, §], Michael Barrow[4], Joan Comenge[5], Lydia Beeken[1], Cai Astley[1], Ilaria Santeramo[1, 2], Claire Hutchinson[3], Lorenzo Ressel[6], Jon Smythe[7], Eric Austin[7], Raphael Levy[5], Matthew J. Rosseinsky[4], Dave J. Adams[8], Harish Poptani[1, 2], B. Kevin Park[3], Patricia Murray[1, 2, *], Bettina Wilm[1, 2, *]

Affiliation:

[1] Department of Cellular and Molecular Physiology, [2] Centre for Preclinical Imaging, [3] Department of Molecular and Clinical Pharmacology, Institute of Translational Medicine, [4] Department of Chemistry, [5] Institute of Integrative Biology, [6] Department of Veterinary Pathology and Public Health, Institute of Veterinary Science, University of Liverpool, Liverpool, UK, [7] NHS Blood and Transplant, Oxford, UK, [8] School of Chemistry, College of Science and Engineering, University of Glasgow, Glasgow, UK,

[§] Authors contributed equally

***** Joint senior/corresponding authors

Author Contributions

L.S., A.T., J.Sh., L.B., C.A.: designed experiments and analysed the data.

M.B., J.C.: produced, characterised and validated contrast agents for MRI and MSOT.

I.S.: isolated and characterised hKCs

J.Sm., E.A.: isolated and characterised hUC-MSCs

L.R.: performed histopathological analysis of tumours

C.H., R.L., M.J.R., D.J.A., H.P., B.K.P.: conceived study and analysed data

P.M., B.W.: conceived study, designed experiments, analysed data and wrote the manuscript.

All authors edited and approved the manuscript.

Abstract

The number of clinical trials using cell-based therapies is increasing, as is the range of cell types being tested, but without a thorough understanding of cell fate and safety. Therefore, there is a pressing need for monitoring of cell fate in preclinical studies to identify potential hazards that might arise in patients. Utilising a unique imaging toolkit combining bioluminescence, optoacoustic and magnetic resonance imaging modalities, we assessed the safety of different cell types by following their biodistribution and persistence in mice. Our imaging studies suggest that the intra-arterial route is more hazardous than intravenous administration. Longitudinal imaging analysis over four weeks revealed that the potential of mouse mesenchymal stem/stromal cells (mMSCs) to form tumours, depended on administration route and mouse strain. Clinically tested human umbilical cord (hUC)-derived MSCs formed growths in 15% of animals that persisted for up to three weeks, indicating a potential tumourigenicity hazard that warrants further testing.

Introduction

Cell-based regenerative medicine therapies (RMTs) have the potential to treat various diseases[1], but the risk of tumour formation is a primary safety concern[2]. Mesenchymal stem/stromal cells (MSCs) isolated from bone marrow, adipose tissue or umbilical cord are being tested in clinical trials, but in many cases, preclinical safety data are not available. Bone marrow-derived MSCs have been used for many years and appear safe[3], but a review of adipose-derived MSCs concluded that while adverse events are rare, they nevertheless do occur, and are likely to be related to underlying health conditions of the patients or administration route[4]. Human umbilical cord-derived (hUC)-MSCs have only recently been introduced in clinical trials, with more than 50% of these initiated within the last 3 years (Supplementary Table 1). hUC-MSCs are less immunogenic than other types of MSCs, which contributes to their attraction as clinical RMTs. However, because of their low immunogenicity in combination with higher proliferative behaviour these cells may

also pose a greater potential risk[5], yet until now, their safety profile has not been robustly assessed. The importance of preclinical safety testing is highlighted by a recent report where a tumour developed in a patient's spinal cord following intrathecal administration of stem cells[6].

The most common way to administer cells systemically in small animals is via the intravenous (IV) route[7], delivering cells directly to the lungs where they are sequestered as a consequence of the pulmonary first-pass effect[8-13]. Although the IV route is also frequently used in clinical trials, administration via the arterial circulation is not uncommon. For instance, clinical trials testing the potential of cell therapies to treat myocardial infarction administer cells into the coronary arteries or left cardiac ventricle[14, 15], while in patients with peripheral artery disease or stroke, intra-arterial injection via the femoral or carotid artery, respectively, is frequently employed[16]. Intra-arterial administration will also lead to systemic distribution to other organs, including the brain, and cells passing through the blood-brain barrier could pose an important safety concern. However, a detailed analysis of cell fate after intra-arterial cell administration has so far not been reported[17].

Non-invasive imaging technologies have opened up exciting new possibilities for preclinical assessment of the safety of cell therapies by monitoring cell biodistribution and persistence through longitudinal *in vivo* cell tracking; however, a platform approach using multimodal imaging for the safety assessment of cells has not been previously implemented. Preclinical imaging technologies for cell tracking, some of which have clinical relevance, include magnetic resonance imaging (MRI) to detect cells labelled with superparamagnetic iron oxide nanoparticles (SPIONs), multispectral optoacoustic tomography (MSOT) to detect cells labelled with gold nanorods or near-infrared red fluorescent protein (iRFP)[18-23], and bioluminescence imaging (BLI) for the detection of cells expressing the genetic reporter, firefly luciferase[24-26]. Genetic reporters are particularly advantageous because signals are only generated from living cells, thus allowing the monitoring of cell proliferation and tumour growth, and avoiding problems based on nanoparticle dissociation from cells, which can lead to false positive signals. However, the spatial resolution of

BLI is poor, making it difficult to precisely locate the cells[24]. By contrast, both preclinical MSOT and MRI have much higher spatial resolution (150 µm and 50 µm, respectively), providing details of the inter- and intra-organ distribution of administered cells. Moreover, as MRI is routinely used in the clinic, it provides a bridge for preclinical and clinical studies.

Here, we have implemented a multi-modal imaging approach comprising BLI, MSOT and MRI, to assess biodistribution and fate of different cell types following venous and arterial administration in healthy mice. Some of these cell types are currently being used in clinical trials, including hUC-MSCs (Supplementary Table 1), kidney-derived cells[27] and macrophages[28]. We show that in a small number of mice, hUC-MSCs started to proliferate over time. Although these hUC-MSC growths eventually regressed, our data raise safety concerns regarding the use of these cells in clinical trials.

Results

Whole body biodistribution of different cell types following intravenous (IV) and intracardiac (IC) administration

Bioluminescence imaging showed that IV delivery of ZsGreen^{+}/Luc^{+} mMSCs, mKSCs, hKCs and hUC-MSCs, resulted in signals exclusively in the lungs, while signals from IV-administered macrophages were also located more posteriorly (Fig. 1a). This was expected because macrophages are known to traverse the lungs and populate other organs, such as the liver and spleen. In contrast, intra-arterial delivery via the left ventricle (from now on referred to as intra-cardiac (IC)) resulted in a whole-body distribution of all cell types (Fig. 1a).

Organ-specific *ex vivo* imaging within 1h of mKSCs being administered IV confirmed the signal was limited to the lungs (Fig. 1b, d). In contrast, after IC administration, bioluminescent signals were detected in the brain, heart, lungs, kidney, spleen, and liver (Fig. 1b, d). A comparable *ex vivo* biodistribution was observed for mMSCs and hKCs following IV and IC administration (not shown),

while with hUC-MSCs, we found low but detectable signals in other organs besides the lungs following IV administration (Supplementary Fig. 1). IV-administered macrophages were found predominantly within the lungs by *ex vivo* imaging (Fig. 1c), but weaker signals were also detected in the spleen and liver (Supplementary Fig. 2), confirming the *in vivo* signal distribution. *Ex vivo* analysis of macrophages after IC injection showed signals in all organs (Fig. 1c, e).

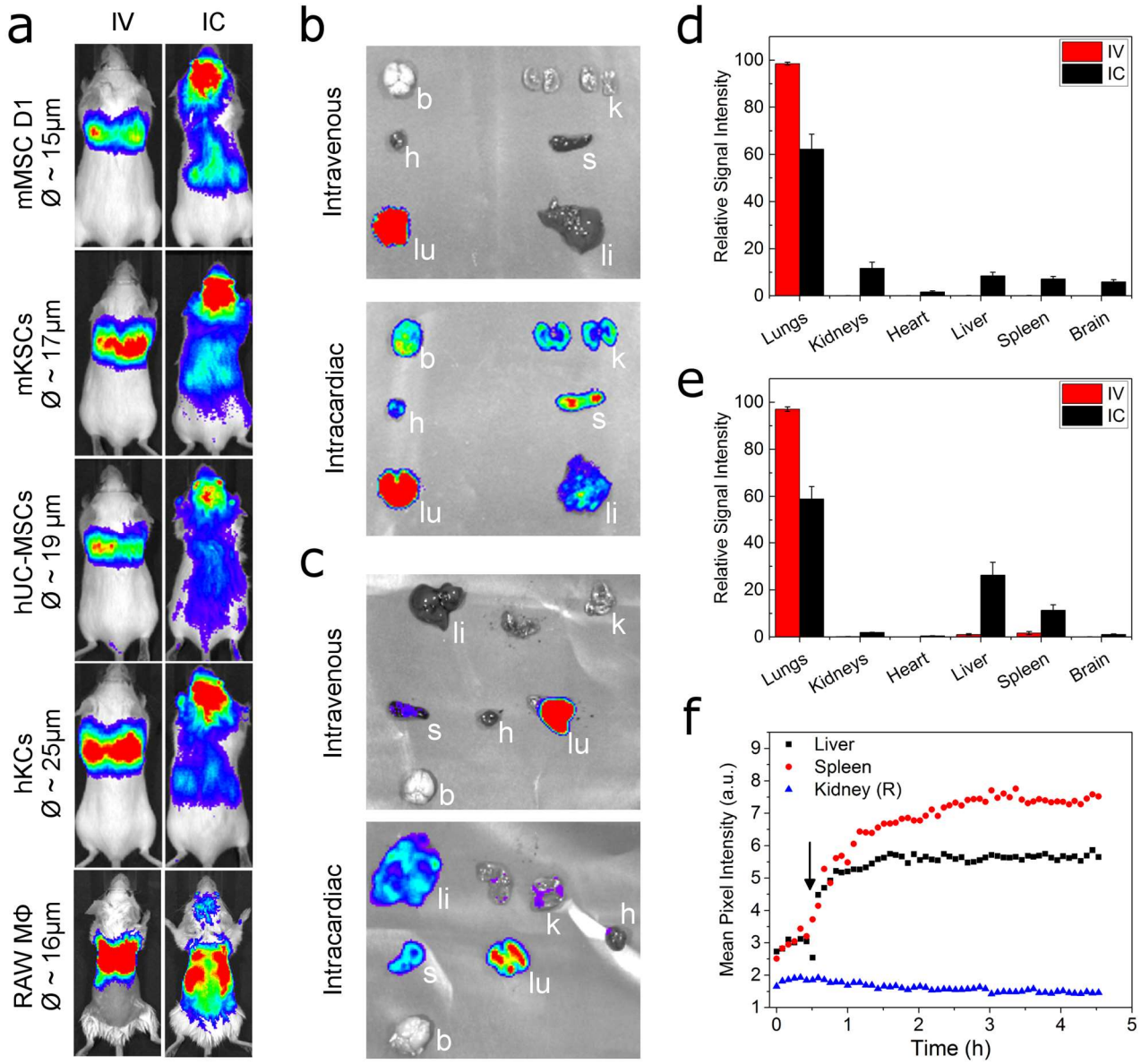

Figure 1. Biodistribution of different cells following intravenous or intracardiac administration. (**a**) BLI immediately after administration, showing that cells were always confined within the lungs after intravenous (IV) administration, but distributed throughout the body after intracardiac (IC) administration; an exception were the macrophages which showed also a more posterior signal after IV administration. Luminescence intensity scale has been adjusted individually for each cell type and is described in Supplementary Table 2. *Ex vivo* bioluminescence imaging of organs within 5h of administration of **(b)** mKSCs or **(c)** macrophages confirmed the *in vivo* cell biodistribution.

Organs are indicated as kidneys (k), spleen (s), liver (li), lungs (lu), heart (h) or brain (b). Quantification of the bioluminescence signal intensity of organs *ex vivo* post **(d)** mKSC or **(e)** macrophage administration. Values represent the mean signal intensity measured in each organ and normalised to the total flux from all organs (*n* = 3 each group). Error bars represent standard error. **(f)** Mean pixel intensity of GNR-labelled macrophages measured via multispectral optoacoustic tomography for a period of 5 hours post IV administration, displaying the kinetics of their accumulation in the spleen and liver. Arrow indicates the time point at which the cells were administered.

To monitor the temporal dynamics of macrophage migration, cells were labelled with GNRs, injected IV, and monitored continuously for 4.5h using MSOT. Signal intensity began to increase immediately in both the liver and spleen until around 90 min (Fig. 1f), but remained close to basal levels in the kidney, consistent with BLI *ex vivo* analysis (Fig. 1e, f). However, when GNR-labelled macrophages were administered IC, increases in signal intensity in the kidney were comparable to those in the liver and spleen 4h post-administration (Supplementary Fig. 3c).

Cell distribution within organs using high-resolution magnetic resonance imaging

Since the spatial resolution of BLI is poor, we used MRI to evaluate the intra-organ biodistribution of ZsGreen$^+$/Luc$^+$/SPION$^+$ mMSCs after IV or IC administration, focussing particularly on the brain and kidneys. Following IC injection, T_2^* weighted imaging revealed hypointense areas distributed homogenously throughout the brain (Fig. 2a), and localised in the cortex of the kidneys (Fig. 2b). However, hypointense contrast was not detected in the brain or kidneys of IV-injected mice, confirming that IV-administration does not deliver mMSCs to either of these organs (Fig. 2a, b). Post mortem MR imaging of extracted organs performed at higher resolution confirmed the hypointense contrast throughout the brain and in the renal cortex of IC-injected mice (Fig. 2a, b).

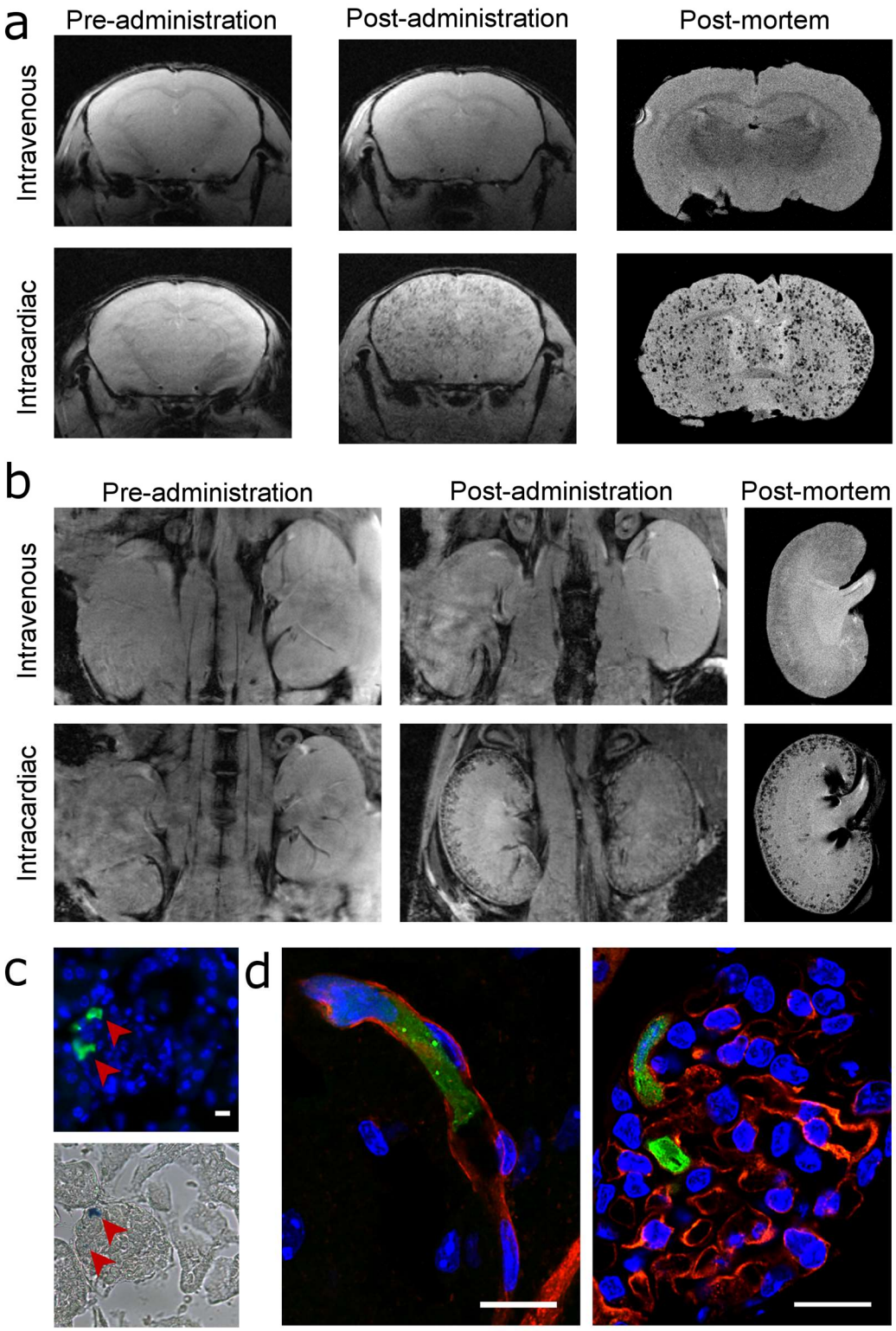

Figure 2. MRI and immunofluorescence images of mMSCs in the brains and kidneys. *In vivo* and post-mortem T_2^*-weighted images of the **(a)** brains and **(b)** kidneys of mice pre- and post-administration of SPION-labelled mMSCs via the IV or IC route. **(c)** Epifluorescence of Zsgreen (green) and nuclei (blue) of a single kidney glomerulus (top) and the corresponding Prussian Blue image (bottom) demonstrating that cells and SPIONs co-localised to the same spatial location. Scale bars correspond to 10 µm. **(d)** Overlay of confocal microscopy images of Isolectin-IB 4 staining (red), ZsGreen (green) and nuclei (blue). Tissue sections were obtained from the brain (left) or kidney (right) of mice that received cells IC.

Histological analysis of ZsGreen expression by fluorescence microscopy in combination with Prussian Blue staining of SPIONs showed that labelled cells were located in the glomeruli (Fig. 2c). ZsGreen and Prussian Blue signals corresponded to the same spatial location, indicating that hypointense contrast *in vivo* was unlikely to result from false-positive detection of SPIONs (e.g. released from dead cells). To determine whether IC-administered cells had undergone extravasation, we performed confocal imaging of IB4-stained blood vessels. This demonstrated that ZsGreen$^+$ mMSCs were physically trapped in the lumen of microcapillaries (Fig. 2d), suggesting that the cells did not cross the blood brain barrier or the glomerular filtration barrier.

Short-term fate of IC-injected cells

To determine how long the cells persisted in major organs we injected 10^6 ZsGreen$^+$/Luc$^+$/SPION$^+$ mMSCs into the left ventricle of BALB/c mice and tracked their fate *in vivo* by MRI and BLI, and post mortem by MRI and fluorescence microscopy (Fig. 3a). On the day of injection, whole-body distribution of IC-administered mMSCs by bioluminescence signals was observed, while in the kidneys, MRI revealed hypointense contrast specifically in the cortex. By 24h, bioluminescence signal intensity decreased, suggesting cell death. Correspondingly, fewer hypointense areas were observed in the renal cortex by MRI, supporting the disappearance of SPION-labelled cells. By 48h, bioluminescence was no longer detectable in the abdominal region, nor was any significant hypointense SPION contrast observed in the kidneys with MRI. This was confirmed by high-resolution MRI of organs *ex vivo*, showing a decrease in contrast in the renal cortex over time, and a decrease in the frequency of ZsGreen$^+$ mMSCs in kidney glomeruli by fluorescence microscopy (Fig. 3a). Changes in the T_2* relaxation time in the renal cortex indicated the relative number of SPION-labelled cells present at each time point. T_2* was significantly lower on the day of cell administration (Fig. 3b) than at baseline but then increased towards baseline levels at 24h and 48h. Because the liver is the major organ for clearance of blood-transported particulates, we quantified

the hepatic T_2* relaxation time, which revealed a subtle but significant decrease from baseline through to 48h (Fig. 3c). These results suggest that following cell death, SPIONs accumulate predominantly in the liver and are not retained by the kidneys.

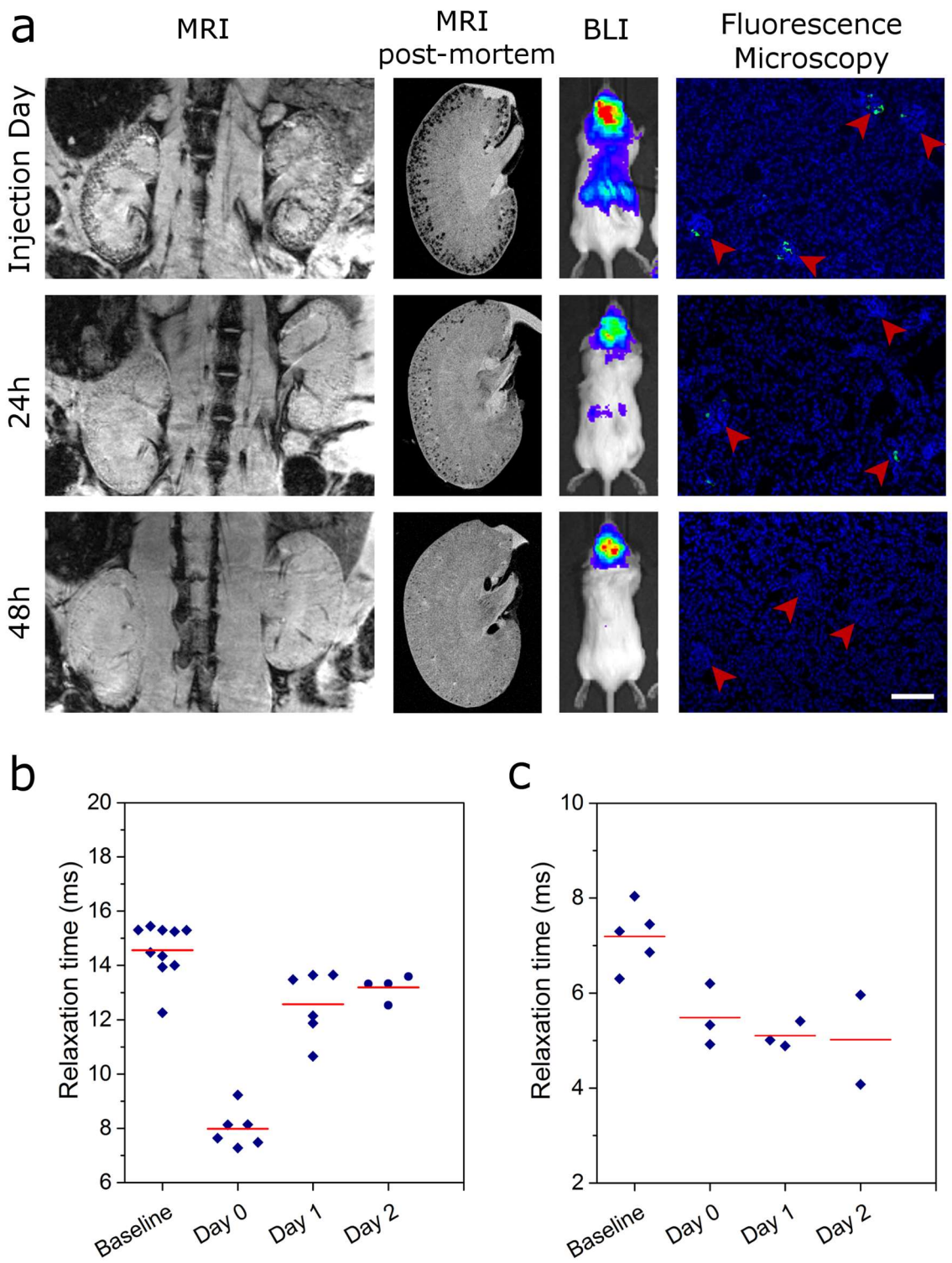

Figure 3. Short-term fate of mMSCs imaged *in vivo* and post-mortem. (a) MRI (*in vivo*, post-mortem), BLI and fluorescence microscopy images of the kidneys immediately, 24h or 48h after IC administration of SPION-labelled mMSCs. Fluorescence images were obtained from tissue sections

where green fluorescence corresponds to ZsGreen expression and blue fluorescence to DAPI staining. Arrowheads indicate individual glomeruli. Scale bar corresponds to 100 µm. T_2^* relaxation time of **(b)** kidney cortices or **(c)** liver before (baseline) and up to 2 days after cell administration. The T_2^* relaxation time in the cortex of the kidney was significantly lower on the day of cell administration (day 0, mean = 7.98 ms +/- SE = 0.29) than at baseline (14.56 +/- 0.32 ms; One-way ANOVA, $p < 0.001$). The T_2^* relaxation time then increased towards baseline levels at day 1 (12.57 +/- 0.50 ms) and day 2 (13.19 +/- 0.23 ms), and by day 2 the difference compared with baseline levels was no longer statistically significant. In the livers, T_2* relaxation time revealed a subtle but significant decrease in relaxation time from baseline through to day 2 (baseline, 7.19 +/- 0.29 ms; day 0, 5.48 +/- 0.38 ms; day 1, 5.10 +/- 0.16 ms; day 2, 5.02 +/- 0.94 ms; One-way ANOVA, $p = 0.006$). See Supplementary Table 3 for Tukey pairwise comparisons.

Effect of administration route on the long-term biodistribution and fate of mMSCs

To assess the effect of administration route on the long-term fate of cells, ZsGreen$^+$/Luc$^+$ mMSCs were administered to BALB/c SCID mice by IC or IV routes, and biodistribution monitored by BLI at multiple time points for 28 days. While both IC and IV injection resulted in the typical immediate biodistribution patterns by 24h (Fig. 1a), by 96h following IV and IC administration, the bioluminescence signal was undetectable, indicating loss of cells via cell death (Fig. 4a). Continued imaging over time showed that bioluminescence signals began to increase again in animals after IC injection from around day 14, consistent with tumour development, but not in animals after IV injection. The increase in signal was particularly prominent in the hindquarters of all five IC-injected mice at day 14, and increased further until day 28 (Fig. 4a, Supplementary Fig. 4a). Detailed analysis of animals after IV administration of mMSCs revealed bioluminescence signals in the lungs of one mouse increased over time (Supplementary Fig. 4b). Overall, whole-body bioluminescence intensity initially decreased following both IC and IV administration, and subsequently increased rapidly in the IC-injected mice (Fig. 4b-d).

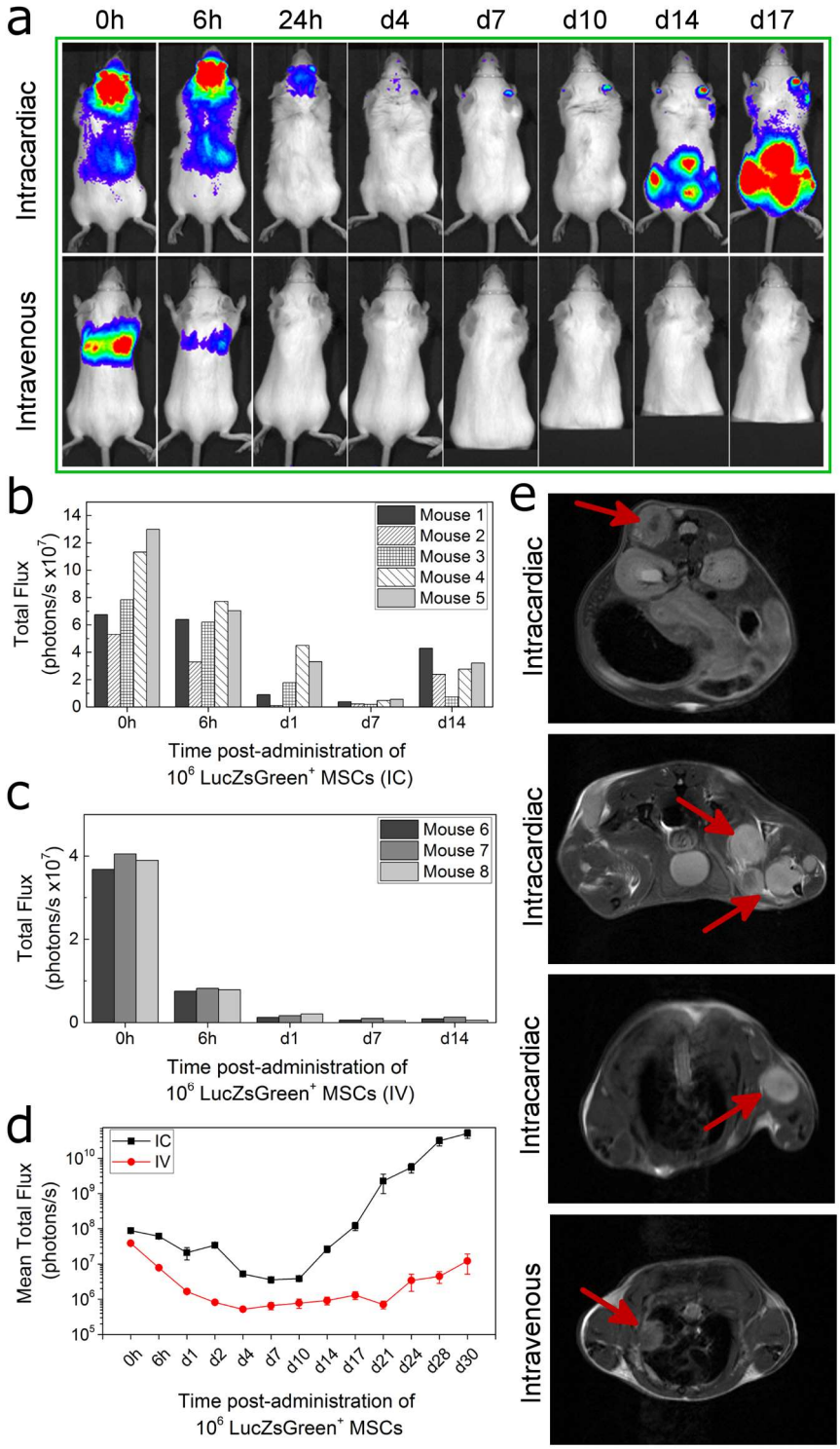

Figure 4. Impact of administration route on long-term tumour formation. (a) Representative BLI of SCID mice administered with mMSC via the IC or IV route. BLI scale corresponds to levels between $1.0x10^5$-$1.0x10^6$ p/s/cm^2/sr. Quantification of the bioluminescence signal from each individual mouse that received mMSCs **(b)** IC (n=5) or **(c)** IV (n=3) up to day 14 (values on day 30 are shown in Supplementary Table 4). Signal corresponds to a region of interest drawn around the whole body of the mouse. **(d)** Mean whole body quantification of the bioluminescence signal up to day 30. Error bars represent SE. **(e)** T_2-weighted MRI of tumours in animals that received mMSCs via each of the different routes (IC or IV). Arrows indicate individual tumours, usually in the skeletal muscle apart from the IV route, where a tumour was found close to the lungs.

Osteosarcoma formation after IC administration of mMSCs

Multiple abnormal growths were present in IC-injected BALB/c SCID mice, predominantly in skeletal muscle surrounding the femurs, but also in muscle near the hips, ribs, and spine (Fig. 5a, f), suggesting tumours had formed. Tumour sites corresponded to foci of intense BL signals which could also be identified using T_2 weighted MR imaging (Fig. 4e). Furthermore, T_2 weighted MR imaging allowed us to detect an abnormal mass in the lungs of one (out of three) IV-injected mouse that displayed an intense bioluminescence signal (Fig. 4e, Supplementary Fig. 4b). Although cells of the mMSC line have been suggested to home to the bone marrow[29], flow cytometry analysis showed the bone marrow was negative for ZsGreen$^+$ cells (Supplementary Fig. 5). Histologically, tumours were characterised by atypical solid proliferation of spindle cells associated with multifocal formation of pale amorphous eosinophilic material (osteoid). The tumours were therefore classified as osteosarcomas (Fig. 5h, j, k). Frozen sections of the tumour tissue exhibited specific ZsGreen fluorescence (Fig. 5i), further confirming the neoplasms originated from mMSCs.

Formation of mMSC-derived tumours in different mouse strains

To determine whether tumours developed because the BALB/c SCID mice were immunocompromised, we investigated the long-term fate of the mMSCs following IC administration in three different immunocompetent mouse strains: BALB/c (same genetic background as mMSCs), FVB (unrelated inbred strain), and MF1 (unrelated outbred strain). The biodistribution immediately after injection was similar between the strains, but at day 28, only the BALB/c mice displayed bioluminescence signals as high as those in the BALB/c SCID mice (Fig. 5b-e). Moreover, the timing and location of tumour formation was consistent in all immunocompetent and immunocompromised BALB/c mice. In the FVB and MF1 strains, mMSC foci tended to form in similar locations as with the BALB/c mice, but bioluminescence signals were weaker. Although

signal intensity gradually increased in FVB mice from d7 to d28, in MF1 outbred mice, signals increased initially up to d21, but then started to decrease as the mMSC foci began to regress.

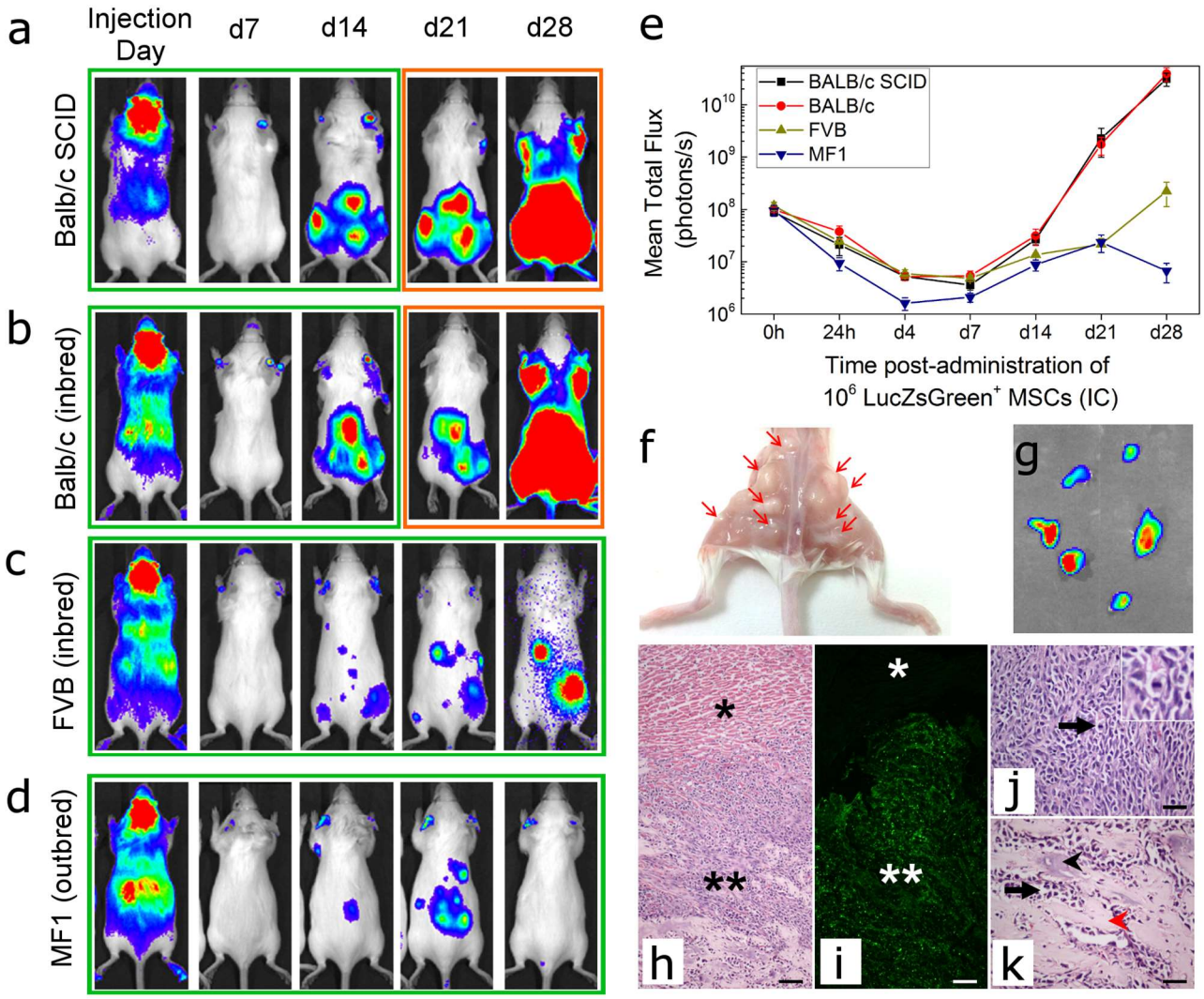

Figure 5. Tumour-formation potential in different mouse strains. Representative BLI of longitudinal tumour monitoring in four strains of mouse following IC administration of mMSCs. **(a)** immunocompromised BALB/c SCID, **(b)** Immunocompetent BALB/c **(c),** FVB or **(d)** MF1 mice. BALB/c mice showed very similar tumour formation potential to BALB/c SCID mice, with respect to timing, size and location of tumour development, requiring a BLI scale two orders of magnitude greater (1.0 x10^7 – 1.0 x10^8 p/s/cm^2/sr, orange frame) than that at 0h (1.0 x10^5 – 1.0 x10^6 p/s/cm^2/sr, green frame) in order to display the strong signals. FVB and MF1 mice displayed weaker BLI foci at d28, and not all animals displayed the same tumour distribution. Data in **(a)** has been partially reproduced from Fig. 4a to facilitate comparison between strains. **(e)** Mean whole body quantification of the bioluminescence signal up to day 30. Error bars represent SE. **(f)** Photograph of the hindquarters of a Balb/c mouse after removal of the skin. Multiple tumour foci are indicated with arrows, demonstrating their presence in the skeletal muscle close to the femurs, hips, and spine. **(g)** BLI of tumours harvested 30 days post-administration of mMSCs confirming that tumours originated from the administered cells and not host tissue (BLI intensity scale 1.0 x10^8 – 1.0 x10^9 p/s/cm^2/sr). **(h-k)** Histological examination of tumour tissue. **(h)** H&E staining and corresponding (**i**) epifluorescence imaging of the ZsGreen reporter. Differences in cell composition

between the tumour (**) and normal tissue (*) are denoted. Scale bars represent 100 µm. **(j, k)** Higher magnification of tumour tissue showing cancer cells arranged in densely cellular monomorphic areas. Scale bars correspond to 50 µm and arrow indicates mitotic figures, one of which is shown in the inset. **(k)** Corresponds to an area where the tumour is moderately cellular with production of unmineralised osteoid (black arrowhead) and partially mineralised matrix (red arrowhead).

Long-term biodistribution of hUC-MSCs in BALB/c SCID mice

Since mMSCs gave rise to tumours in immuno-compromised and –competent mice predominantly after systemic arterial injection, we were concerned that clinically relevant MSCs could carry a similar health risk. We focussed on hUC-MSCs as they are currently being used in an increasing number of clinical trials (Supplementary Table 1). When following the fate of IV- and IC-administered hUC-MSCs in BALB/c SCID mice, we found that in most cases, BLI signals became weaker within a few days of administration, and remained undetectable for the duration of the study (8 weeks) (Fig. 6a, b). However, in a small number of mice (~15%) UC-MSC foci had developed in locations outside the major organs (Fig. 6c, red arrows). Although these foci initially expanded, they then appeared to regress, and by d21 were barely detectable, and did not reappear during the remaining 5 weeks of the experiment.

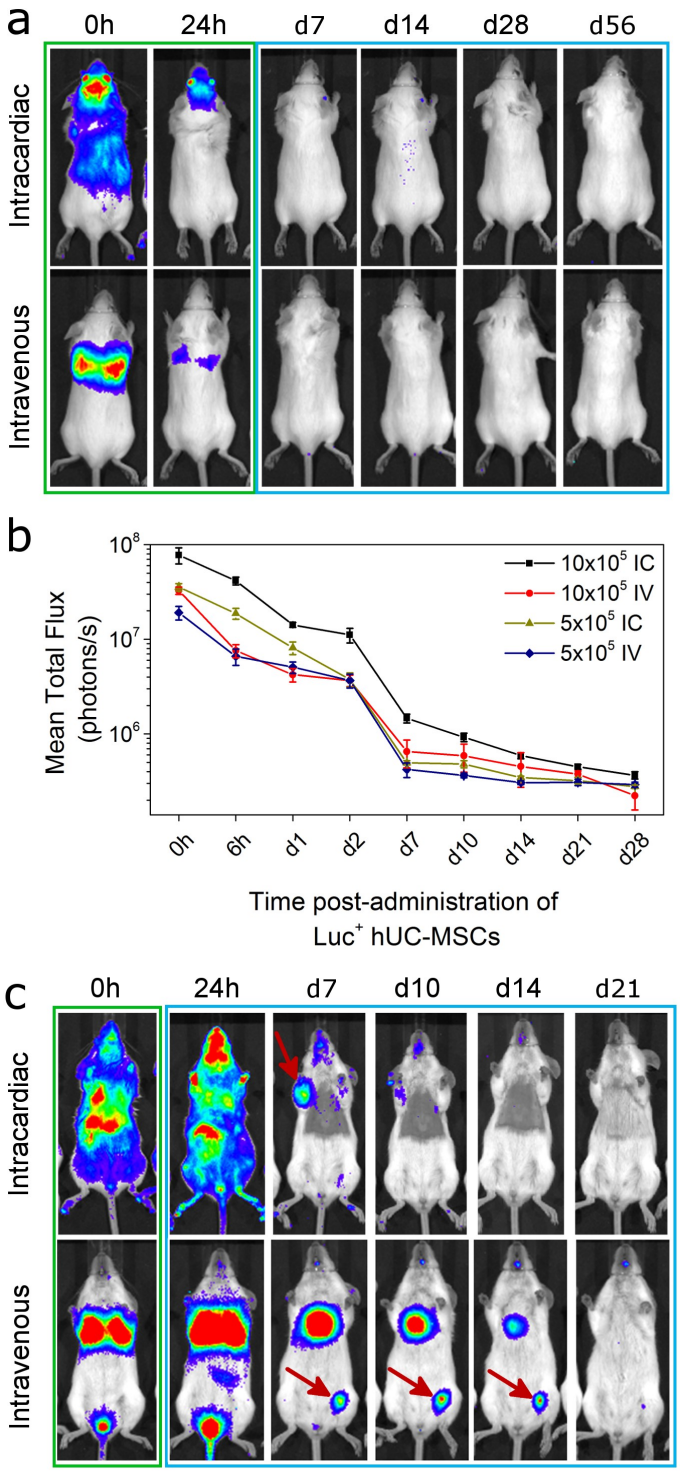

Figure 6. Long-term monitoring of human umbilical-cord derived MSCs in Balb/c mice. (a) Representative BLI of mice administered with 10^6 hUC-MSC via the IC or IV route. The signal was progressively lost shortly after administration, with no evidence of malignant growth. **(b)** Mean whole body quantification of the bioluminescence signal up to day 28 as obtained with two different cell doses. Error bars represent SE. **(c)** BLI images from mice that displayed signal that persisted up to or beyond day 7 (dose: 10^6 cells, ventral orientation). In all cases, the signals had disappeared by day 21 and not returned by day 56. Images in blue frames **(a, c)** are presented in a lower intensity scale (1.0×10^4 – 1.0×10^5 p/s/cm^2/sr) to display weaker signals.

Discussion

Here, we have employed a novel platform approach of non-invasive preclinical imaging encompassing BLI, MRI and MSOT to assess the biodistribution and persistence of a range of mouse and human cell types following IV and IC administration in healthy mice. These cells included mouse MSCs, kidney stem cells and macrophages, as well as human kidney-derived cells and hUC-MSCs, the latter being already tested as cell therapies in clinical trials. As expected, immediate analysis after IV administration revealed that apart from macrophages, all other cell types were mostly sequestered in the lungs, although small numbers of hUC-MSCs could be detected in other organs following *ex vivo* analysis. After IC administration, all cell types showed a widespread distribution. However, irrespective of the administration route, analysis using all three imaging technologies determined that cells disappeared from major organs within 24-48 hours, which based on the loss of BLI signals, was likely due to cell death. The observation that cells are cleared very quickly from the major organs following IC administration indicates that the arterial route poses no significant advantage for cell therapy administration. By contrast, our long-term tracking analysis over four to eight weeks, provides the first evidence that arterial administration of cells may carry a higher tumourigenicity hazard. Therefore, this striking finding suggests that IV administration of cell therapies is safer for clinical applications. We thus recommend that further investigations are urgently needed before conducting clinical trials where cells are delivered arterially.

Our platform of imaging techniques was also able to provide some mechanistic insight into the fate of cells after administration. Macrophages have been previously shown to home to the liver and spleen after passage through the lungs[30]. However, the dynamics of this homing process had not been described. Using multi-modal BLI and MSOT, we could monitor macrophage accumulation in the liver and spleen for 4.5h continuously at high spatial resolution. We found that labelled macrophages immediately started to accumulate in liver and spleen, particularly in

the first ~90 min, which indicated that some of the macrophages instantly passed through the pulmonary circulation.

While BLI has the advantage of highly sensitive body-wide detection of luciferase-expressing cells, its spatial resolution is poor, which prevents organ-focussed imaging. To visualise cells within major organs such as kidney and brain, and monitor their fate over time, we implemented a bimodal approach comprising BLI and MRI, taking advantage of the high spatial resolution of MRI in addition to the high sensitivity of BLI and the fact that luciferase activity is dependent on cell viability[20-22, 24]. Detailed analysis of the biodistribution of mMSCs after IC injection using *in vivo*, and subsequently *ex vivo* MR imaging techniques revealed that SPION-labelled cells were scattered throughout the brain, while in the kidneys, they were restricted to the cortical regions. *Ex vivo* histological staining and fluorescence microscopy demonstrated that cells in the kidneys were found only within the glomeruli, bounded by endothelial cells within the microvasculature. Similarly, cells in the brain were only localised within the microvasculature, indicating that they lack the capacity to pass through the blood brain barrier. These results demonstrate that the mMSCs cannot extravasate into the brain and kidneys, and are in line with our observation that tumours were not found in these organs after four weeks.

Surprisingly, during long-term cell tracking of the BALB/c-derived mMSCs, we observed tumour formation in skeletal muscle following IC administration to a similar degree in immune-competent BALB/c mice as in BALB/c SCIDs. mMSCs also gave rise to tumours in an unrelated inbred strain, albeit at a slower rate, while in an unrelated outbred strain, small foci of mMSCs expanded at early time points and later regressed. Taken together, these data suggest that the adaptive immune system might not be able to recognise tumours derived from syngeneic MSCs (equivalent to autologous MSCs in human applications), and that the genetic background of the host appears to have an effect on the propensity of MSCs to form tumours. This could be a concern for human trials using autologous MSCs where the ability of the cells to form tumours may not be detected

by the recipient's immune system. Furthermore, the results suggest that the risk of tumour formation might depend on undefined genetic factors that would vary from patient to patient.

Our observation that mMSCs distributed to most organs following IC injection, but tumours were predominantly localised in the skeletal muscles and not within the organs they originally appeared in, raises the question of how tumour formation is regulated in different organs and tissues. Our data indicate that the cells had a 'survival advantage' in muscular tissue, but not in the brain and the kidneys, from which they failed to extravasate. We hypothesise that following IC administration, a small number of MSCs were able to extravasate from the capillaries in the skeletal muscle where they started to proliferate. The mechanisms that regulate the ability of the mMSCs to extravasate and form tumours in the skeletal muscle but not in other organs are not known, and further analysis is required to determine the molecular and cellular factors controlling this process. Our results also show that the cells failed to home to and populate the bone marrow, which is surprising given the cells had been originally isolated from the bone marrow[31]. The D1 mMSC line used here has not previously been reported to generate invasive tumours, since subcutaneously injected cells provided no evidence of metastasing, even if they proliferated at the injection site[32, 33]. Our observation that the mMSCs did not form tumours outside the lung following IV administration is therefore consistent with this finding.

Since these observations suggested that arterial administration of MSC-based cell therapies could have important safety implications, we followed the fate of hUC-MSCs, which are currently being used in several clinical trials (Supplementary Table 1). While in most animals the cells became undetectable within a few days after IV administration, in a few mice the cells persisted longer, albeit transiently, in other body regions where their presence was not expected. We suggest that this unusual behaviour is not linked to cell size, because the hUC-MSCs were not smaller than mKSCs or mMSCs, but could possibly be due to their surface proteins, allowing some of the cells to escape the lungs[11, 34]. The observation that hUC-MSC foci appeared in a small number of mice,

grew in size, but later disappeared, was difficult to explain, especially given that the mice were SCIDs and thus lacked an adaptive immune system. It is possible that the cells eventually elicited a xenogeneic response involving macrophages and natural killer cells[35], after initially suppressing the native immune system, which is one of their central properties[36, 37]. Alternatively, the hUC-MSCs may have expanded in the animal but then become senescent and died, irrespective of the host's ability to mount an immune response. Thus, after an 8-week period of cell tracking, we could not observe any tumour growth by *in vivo* or *ex vivo* BLI in all SCID mice to which hUC-MSCs had been administered by either IV or IC injection. However, the observation that the hUC-MSCs persisted for a time period in some immunodeficient animals indicates that these cells carry greater safety risks and suggests that clinical therapies with these cells should proceed with caution with appropriate risk management plan. Further preclinical studies are needed to determine the mechanisms by which hUC-MSCs were able to persist as well as eventually disappear in order to better define the potential for tumourigenicity. The imaging platform developed herein provides the necessary biotechnology for preclinical evaluation of the potential tumourigenicity of cell products used for cell transplantation, for which there is presently no internationally recognised guideline.

Acknowledgements:

The authors would like to thank Carmel Moran and Adrian Thomson, University of Edinburgh, for providing help and technical guidance in optimising the US-IC injection method, and Thomas Wilm, University of Liverpool, for help with the confocal imaging. All *in vivo* imaging was carried out in the Centre for Preclinical Imaging, University of Liverpool. We gratefully acknowledge support by the MRC, EPSRC and BBSRC-funded UK Regenerative Medicine Platform "Safety and Efficacy, focussing on Imaging Technologies Hub" (MR/K026739/1), by a Marie Curie Fellowship to Joan Comenge (NANOSTEMCELLTRACKING), and by the FP7 Marie Curie Initial Training Network

'NephroTools' and Alder Hey Children's Kidney Fund. Cai Astley and Lydia Beeken were self-funded in this project.

Online Methods

Animals

Mice (Charles River, UK) were housed in individually ventilated cages under a 12 hour light/dark cycle, with *ad libitum* access to standard food and water. All animal experiments were performed under a licence granted under the Animals (Scientific Procedures) Act 1986 and were approved by the University of Liverpool ethics committee. Experiments are reported in line with the ARRIVE guidelines. Tumour formation was closely monitored and the tumour burden was not allowed to exceed the recommended size[38].

Cell Preparation

Mouse kidney-derived stem cells (mKSCs)[39], the D1 mouse MSC (mMSC) line (D1 ORL UVA [D1](ATCC® CRL-12424™)), primary human umbilical cord-derived MSCs (hUC-MSCs; collected from consenting donors and produced identically to those already being used in clinical trials by NHS Blood and Transplant NHSBT), human kidney cells (hKCs; kidneys deemed unsuitable for transplantation via UK NHSBT[10]) and RAW264.7 macrophages (European Collection of Authenticated Cell Cultures 91062702) were cultured at 37°C under a humidified atmosphere with 5% CO_2 (Supplementary Table 5).

For detection by BLI, cells were transduced with a lentiviral vector encoding either firefly luciferase (Luc) or a bicistronic construct of Luc and ZsGreen, all under control of the constitutive promoter EF1a. The vector plasmids were a gift from Bryan Welm (Addgene plasmids # 21375 and 39196) and the production of viral particles and cell transduction was carried out as previously described[40, 41]. The mKSCs were infected with a multiplicity of infection (MOI) of 10, whereas all

other cells were infected with an MOI of 5. At least 90% of the cell populations expressed the vector after transduction, except for macrophages, which did not tolerate polybrene and thus displayed a reduced infection efficiency. Cell sorting based on ZsGreen fluorescence obtained a macrophage population that was 100% positive for the luciferase construct.

Average cell diameter was estimated by measuring the volume of a cell pellet in a packed cell volume (PCV) tube according to the manufacturer's instructions (Techno Plastic Products, Switzerland). The cell diameter was calculated using the formula:

$$\emptyset_{cell} = 2 \times \sqrt[3]{\frac{3\,{}^{V}/_{c}}{4\pi}}$$

where V corresponds to the pellet volume, and c to the number of cells in the pellet.

For MR tracking, cells were labelled with diethylaminoethyl-dextran coated SPIONs synthesised in house as previously described[42, 43]. SPIONs were added to the culture medium at a concentration of 25 µg[Fe]/mL 24h prior to the experiment, after which cells were washed to remove excess particles and harvested for administration as described below. This resulted in iron content of ~ 6 pg[Fe]/cell.

GNRs were synthesised using a protocol first reported by El-Sayed's group[44] and coated with silica as described by Comenge *et al.*[32]. Macrophages were labelled for 24h with GNRs at a final concentration of 10 pM before harvesting for cell injection. This concentration caused no reduction in cell viability.

Cell administration

Cells were trypsinised, pelleted, resuspended in ice-cold phosphate buffered saline (PBS) and kept on ice until injection. 100µl cell suspension was administered to mice via intravenous (IV) or

ultrasound-guided intracardiac (IC, left ventricle, Supplementary Fig. 6) injection. Detailed information and comments on the IC administration method are provided in the SI.

Bioluminescence imaging

Short-term study: ZsGreen$^+$/Luc$^+$ mMSCs, mKSCs, hKCs, macrophages or Luc$^+$ hUC-MSCs were administered IV or IC to BALB/c mice. Long-term study: ZsGreen$^+$/Luc$^+$ mMSCs or Luc$^+$ hUC-MSCs were administered by IV or IC to BALB/c (severe combined immunodeficient) SCID mice (see Table 1 for experimental details). The *in vivo* biodistribution of cells was monitored by BLI immediately after cell administration, and at multiple time points up to 30 days. Mice were administered 150 mg/kg body weight (BW) luciferin (subcutaneous, SC) (Promega, UK), and imaged 15 min later in a bioluminescence imager (IVIS Spectrum, Perkin Elmer, UK). Imaging data were normalised to the acquisition conditions and expressed as radiance (photons/second/cm^2/steradian (p/s/cm^2/sr)), and the scale was adjusted according to the strength of signal detected. To facilitate the comparison of bioluminescence images with different scales, coloured frames were used to indicate the scale ranges (Supplementary Table 6).

Table 1. Experimental details of studies, mouse strains, cell types, route of administration, dose and number of animals studied

Study	**Mouse strain**	**Cell Type**	**Route**	**Dose**	**Number of animals**
BLI short-term biodistribution (and MSOT for RAW macrophages)	BALB/c	mMSC	IV and IC	1.0×10^6	Minimum n = 3 for each cell type and administration route
	BALB/c	mKSC	IV and IC	1.0×10^6	
	BALB/c	hUC-MSC	IV and IC	3.0×10^5	
	BALB/c	hKC	IV and IC	1.0×10^6	
	BALB/c	macrophages	IV and IC	1.0×10^7	
BLI long-term biodistribution	BALB/c SCID	mMSC	IV	1.0×10^6	n = 3
	BALB/c SCID	mMSC	IC	1.0×10^6	n = 5
	BALB/c	mMSC	IC	1.0×10^6	n = 4
	FVB	mMSC	IC	1.0×10^6	n = 4
	MF1	mMSC	IC	1.0×10^6	n = 4
	BALB/c SCID	hUC-MSC	IV	1.0×10^6	n = 5
	BALB/c SCID	hUC-MSC	IC	1.0×10^6	n = 3
	BALB/c SCID	hUC-MSC	IV	5.0×10^5	n = 6
	BALB/c SCID	hUC-MSC	IC	5.0×10^5	n = 6
MRI cell tracking	BALB/c	mMSC	IV	1.0×10^6	n = 2
	BALB/c	mMSC	IC	1.0×10^6	n = 7

At the respective study end points, mice were culled and organs with any visibly identifiable tumours imaged *ex vivo* by BLI. Kidneys were cut coronally for *ex vivo* imaging, and all other organs were imaged whole. Bioluminescence signals of whole live mice or individual organs ex vivo were

quantified by drawing regions of interest (ROIs) from which the total flux (photons/second) was obtained. The relative signal intensity from each organ was calculated as a percentage of the signal intensity from all organs. For *ex vivo* kidney imaging, the ROI was drawn around all four kidney halves and a single value for total bioluminescence signal was recorded.

Multispectral Optoacoustic Tomography (MSOT)

MSOT was carried out using the inVision 256-TF MSOT imaging system (iThera Medical, Munich). Images were recorded at the following wavelengths: every 10 nm from 660 nm and 760nm, and every 20 nm from 780 nm and 900 nm, at a rate of 10 frames per second and averaging 10 consecutive frames. All mice were allowed to adjust to the imaging system for 15 minutes prior to recording data. For monitoring biodistribution of macrophages after IV administration, a 15 mm section of the abdomen to include the liver, kidneys and spleen of the mice was imaged repeatedly for a total of 4.5 hours; 30 minutes into the imaging the BALB/c mice (n = 3) received 10^7 macrophages via a tail vein catheter. For the IC imaging a 15 mm section of the abdomen was imaged once, followed by an ultrasound (Prospect 2.0, S-Sharp, Taipei city) guided injection of 10^7 macrophages into the left ventricle of the heart of 3 BALB/c mice. Mice were then returned to the photoacoustic imaging system for imaging as previously described. Data was reconstructed and multispectral processing was performed to resolve signals in the liver, kidney and spleen for GNRs. Regions of interest were drawn around the liver, right kidney and spleen (Supplementary Fig. 3) to generate mean pixel intensity data.

MR imaging

ZsGreen$^+$/Luc$^+$/SPION$^+$ mMSCs (10^6) were administered to BALB/c mice IV (*n* = 2) or IC (*n* = 2 for short-term analysis; *n* = 5 for longitudinal tracking). The biodistribution of cells in the brain and kidney was imaged with a Bruker Avance III spectrometer interfaced to a 9.4T magnet system

(Bruker Biospec 90/20 USR) using a Fast Low-Angle Shot (FLASH) T_2* weighted sequence at baseline and up to 2 days post administration. T_2* relaxation times were obtained from a T_2* map generated with a multi-gradient echo (MGE) sequence by drawing ROIs around the cortex of the kidney (Supplementary Fig. 7) or a region of the liver. At least one animal was culled at each time point for histological analyses, and brains and kidneys were fixed with 4% formaldehyde and imaged at a higher resolution *post mortem* (all MR acquisition parameters are described in the Supplementary Table 7). Tumours were imaged with a T_2 weighted fast spin echo sequence.

Histopathological analysis

Perfusion fixed frozen brain and kidney sections were stained for the endothelial cell marker isolectin B4 (IB4, L2140, Sigma Aldrich, UK) as described previously[45]. The presence of ZsGreen$^+$ mMSCs within brain and glomerular capillaries was imaged by confocal microscopy (LSM 800 Airyscan, Zeiss). Frozen kidney sections (7µm) were stained for the presence of iron (Iron Stain Kit, Sigma, UK) according to manufacturer's instructions to detect SPIONs, and consecutive sections were counterstained with DAPI. Prussian blue stained cells and ZsGreen-positive mMSCs were imaged by bright field and epifluorescence microscopy.

Tumours were fixed in 4% paraformaldehyde at 4°C for 24h, washed in PBS and processed through an ethanol and xylene series before embedding in paraffin. 5 µm tissue sections were stained for haematoxylin and eosin (H&E) by standard methods and morphologically assessed.

Fluorescence activated cell sorting (FACS)

Bone marrow was extracted as previously described[46]. In short, femurs and tibias were collected in PBS containing penicillin/streptomycin, bone marrow flushed out with PBS, centrifuged (400 g, 5 mins) and then resuspended in fresh PBS before analysis by FACS for ZsGreen expression.

Statistical Analyses

Statistical analyses were performed using Minitab 17 statistical software. A one-way ANOVA (analysis of variance) was used to compare multiple groups. When an ANOVA resulted in a statistically significant result ($p < 0.05$), a Tukey pairwise comparison was performed in order to determine which groups were significantly different. The Tukey pairwise comparison assigned each group at least one letter, and groups that did not share a letter were significantly different from one another.

References:

1. Buzhor, E. et al. Cell-based therapy approaches: The hope for incurable diseases. *Regenerative Medicine* **9**, 649-672 (2014).
2. Heslop, J.A. et al. Concise review: workshop review: understanding and assessing the risks of stem cell-based therapies. *Stem Cells Transl Med* **4**, 389-400 (2015).
3. Lalu, M.M. et al. Safety of cell therapy with mesenchymal stromal cells (SafeCell): a systematic review and meta-analysis of clinical trials. *PloS one* **7**, e47559 (2012).
4. Toyserkani, N. et al. Concise Review: A Safety Assessment of Adipose-Derived Cell Therapy in Clinical Trials: A Systematic Review of Reported Adverse Events: Safety of Adipose-Derived Cell Therapy. (2017).
5. Li, X. et al. Comprehensive characterization of four different populations of human mesenchymal stem cells as regards their immune properties, proliferation and differentiation. *International journal of molecular medicine* **34**, 695-704 (2014).
6. Berkowitz, A.L. et al. Glioproliferative Lesion of the Spinal Cord as a Complication of "Stem-Cell Tourism". *New England Journal of Medicine* **375**, 196-198 (2016).
7. Papazova, D.A. et al. Cell-based therapies for experimental chronic kidney disease: a systematic review and meta-analysis. *Disease models & mechanisms* **8**, 281-293 (2015).
8. Schrepfer, S. et al. Stem Cell Transplantation: The Lung Barrier. *Transplantation Proceedings* **39**, 573-576 (2007).
9. Lee, R.H. et al. Intravenous hMSCs improve myocardial infarction in mice because cells embolized in lung are activated to secrete the anti-inflammatory protein TSG-6. *Cell stem cell* **5**, 54-63 (2009).
10. Santeramo, I. et al. Human kidney-derived cells ameliorate acute kidney injury without engrafting into renal tissue. *Stem Cells Translational Medicine* **6**, 1373–1384 (2017).
11. Leibacher, J. & Henschler, R. Biodistribution, migration and homing of systemically applied mesenchymal stem/stromal cells. *Stem Cell Research & Therapy* **7**, 7 (2016).
12. Eggenhofer, E. et al. Mesenchymal stem cells are short-lived and do not migrate beyond the lungs after intravenous infusion. *Frontiers in Immunology* **3**, 297 (2012).
13. Fischer, U.M. et al. Pulmonary passage is a major obstacle for intravenous stem cell delivery: the pulmonary first-pass effect. *Stem cells and development* **18** (2009).
14. Combination Stem Cell (MESENDO) Therapy for Utilization and Rescue of Infarcted Myocardium. https://clinicaltrials.gov Identifier No NCT00548613 (2011).
15. EXpanded CELL ENdocardiac Transplantation (EXCELLENT) https://clinicaltrials.gov Identifier No NCT02669810 (2017).
16. Walter, D.H. et al. Intraarterial administration of bone marrow mononuclear cells in patients with critical limb ischemia: a randomized-start, placebo-controlled pilot trial (PROVASA). *Circ Cardiovasc Interv* **4**, 26-37 (2011).
17. Toyserkani, N.M. et al. Concise Review: A Safety Assessment of Adipose-Derived Cell Therapy in Clinical Trials: A Systematic Review of Reported Adverse Events. *Stem Cells Translational Medicine* **6**, 1786-1794 (2017).
18. Taylor, A., Wilson, K.M., Murray, P., Fernig, D.G. & Levy, R. Long-term tracking of cells using inorganic nanoparticles as contrast agents: are we there yet? *Chemical Society reviews* **41**, 2707-2717 (2012).
19. Kircher, M.F., Gambhir, S.S. & Grimm, J. Noninvasive cell-tracking methods. *Nat Rev Clin Oncol* **8**, 677-688 (2011).
20. Paley, M.A. & Prescher, J.A. Bioluminescence: a versatile technique for imaging cellular and molecular features. *MedChemComm* **5**, 255-267 (2014).

21. Lyons, S.K., Patrick, P.S. & Brindle, K.M. Imaging mouse cancer models in vivo using reporter transgenes. *Cold Spring Harbor protocols* **2013**, 685-699 (2013).
22. Scarfe, L. et al. Preclinical imaging methods for assessing the safety and efficacy of regenerative medicine therapies. *npj Regenerative Medicine* **In Press** (2017).
23. Comenge, J. et al. Multimodal cell tracking from systemic administration to tumour growth using gold nanorods and reporter genes. *bioRxiv*, DOI 10.1101/199836 (2017).
24. Kim, J.E., Kalimuthu, S. & Ahn, B.-C. In Vivo Cell Tracking with Bioluminescence Imaging. *Nuclear Medicine and Molecular Imaging* **49**, 3-10 (2015).
25. Togel, F., Yang, Y., Zhang, P., Hu, Z. & Westenfelder, C. Bioluminescence imaging to monitor the in vivo distribution of administered mesenchymal stem cells in acute kidney injury. *American journal of physiology. Renal physiology* **295**, F315-321 (2008).
26. Wise, A.F. et al. Human mesenchymal stem cells alter macrophage phenotype and promote regeneration via homing to the kidney following ischemia-reperfusion injury. *American journal of physiology. Renal physiology* **306**, F1222-1235 (2014).
27. Autologous Neo-Kidney Augment (NKA) in Patients With Type 2 Diabetes and Chronic Kidney Disease (CKD). https://clinicaltrials.gov Identifier No NCT02525263 (2017).
28. Safety of Autologous M2 Macrophage in Treatment of Non-Acute Stroke Patients. https://clinicaltrials.gov Identifier No NCT01845350 (2016).
29. Balian, G., Wang, G.J., Diduch, D. & Hahn, C. Pluripotential bone marrow cell line and methods of using the same. US Patent US6082364 A (2000).
30. Dou, H. et al. Development of a macrophage-based nanoparticle platform for antiretroviral drug delivery. *Blood* **108**, 2827-2835 (2006).
31. Diduch, D.R., Coe, M.R., Joyner, C., Owen, M.E. & Balian, G. Two cell lines from bone marrow that differ in terms of collagen synthesis, osteogenic characteristics, and matrix mineralization. *J Bone Joint Surg Am* **75**, 92-105 (1993).
32. Comenge, J. et al. Preventing Plasmon Coupling between Gold Nanorods Improves the Sensitivity of Photoacoustic Detection of Labeled Stem Cells in Vivo. *ACS Nano* **10**, 7106-7116 (2016).
33. Juffroy, O. et al. Subcutaneous graft of D1 mouse mesenchymal stem cells leads to the formation of a bone-like structure. *Differentiation; research in biological diversity* **78**, 223-231 (2009).
34. Karp, J.M. & Leng Teo, G.S. Mesenchymal stem cell homing: the devil is in the details. *Cell stem cell* **4** (2009).
35. Xu, X.C., Goodman, J., Sasaki, H., Lowell, J. & Mohanakumar, T. Activation of natural killer cells and macrophages by porcine endothelial cells augments specific T-cell xenoresponse. *Am J Transplant* **2**, 314-322 (2002).
36. Barcia, R.N. et al. What Makes Umbilical Cord Tissue-Derived Mesenchymal Stromal Cells Superior Immunomodulators When Compared to Bone Marrow Derived Mesenchymal Stromal Cells? *Stem Cells Int* **2015**, 583984 (2015).
37. Gao, F. et al. Mesenchymal stem cells and immunomodulation: current status and future prospects. *Cell Death Dis* **7**, e2062 (2016).
38. Workman, P. et al. Guidelines for the welfare and use of animals in cancer research. *Br J Cancer* **102**, 1555-1577 (2010).
39. Fuente Mora, C. et al. Differentiation of podocyte and proximal tubule-like cells from a mouse kidney-derived stem cell line. *Stem cells and development* **21**, 296-307 (2012).
40. Taylor, A. et al. Assessing the efficacy of nano- and micro-sized magnetic particles as contrast agents for MRI cell tracking. *PloS one* **9**, e100259 (2014).
41. Kutner, R.H., Zhang, X.Y. & Reiser, J. Production, concentration and titration of pseudotyped HIV-1-based lentiviral vectors. *Nature protocols* **4**, 495-505 (2009).

42. Barrow, M. et al. Co-precipitation of DEAE-dextran coated SPIONs: how synthesis conditions affect particle properties, stem cell labelling and MR contrast. *Contrast Media and Molecular Imaging* **11**, 362-370 (2016).
43. Barrow, M. et al. Tailoring the surface charge of dextran-based polymer coated SPIONs for modulated stem cell uptake and MRI contrast. *Biomaterials Science* **3**, 608-616 (2015).
44. Nikoobakht, B. & El-Sayed, M.A. Preparation and growth mechanism of gold nanorods (NRs) using seed-mediated growth method. *Chemistry of Materials* **15**, 1957-1962 (2003).
45. Wälchli, T. et al. Quantitative assessment of angiogenesis, perfused blood vessels and endothelial tip cells in the postnatal mouse brain. *Nat. Protocols* **10**, 53-74 (2015).
46. Sharkey, J. et al. Functionalized superparamagnetic iron oxide nanoparticles provide highly efficient iron-labeling in macrophages for magnetic resonance-based detection in vivo. *Cytotherapy* **19**, 555-569 (2017).